Validation of histogram-based virtual source models for different IGRT kV-imaging systems

Guillaume Boissonnat, Helena Chesneau, Eric Barat, Thomas Dautremer, Juan-Carlos García Hernández, Delphine Lazaro

Validation of histogram-based virtual source models for different IGRT kV-imaging systems

G. Boissonnat[1a], J.-C.Garcia-Hernandez[1], E. Barat[1], T. Dautremer[1], H. Chesneau[1] and D. Lazaro[1]

[1]CEA, LIST, System Modelling and Simulation Lab, F-91191 Gif-sur-Yvette, France

[a)] Corresponding author : guillaume.boissonnat@cea.fr

Abstract

Purpose: The increased use of kilovoltage imaging in Image-Guided RadioTherapy (IGRT) raises the need to inquire the additional imaging doses. In that framework, we propose to use Monte Carlo-based virtual sources to model four different kV imaging systems used in radiotherapy, namely Varian OBI, Elekta XVI, Brainlab ExacTrac, and Accuray Cyberknife.

Methods: In this study, first, the overall methodology to build the virtual source models (VSM) was described and thoroughly validated against standard phase-space files calculated using Monte Carlo simulations of the XVI system. Last, each modeled system was compared to profiles and depth-dose-curve measurements performed in homogeneous phantom.

Results: Comparisons between PSF-based and VSM-based calculations highlighted that VSMs could provide equivalent dose results (within 1% of difference) than PSFs inside the imaging field-of-view (FOV). In contrast, VSMs tend to underestimate (for up to 20%) calculated doses outside of the imaging FOV due to the assumptions underlying the VSM construction. In addition, we showed that the use of VSMs allows reducing calculation time by at least a factor of 2.8. Indeed, statistical uncertainties on dose distributions computed using VSMs were much lower than those obtained from PSF-based calculations.

Conclusions: For each of the four imaging systems, VSMs were successfully validated against measurements in homogeneous phantom, and are therefore ready to be used for future preclinical studies in heterogeneous or anthropomorphic phantoms. They should enable, later on, to estimate precisely patient specific 3D dose maps delivered during kV-imaging procedures.

Key words: IGRT, Monte Carlo dose calculation, virtual source model

Introduction

Kilovoltage imaging has become an essential tool throughout image-guided radiotherapy (IGRT) treatments, and is available in the form of different imaging systems depending on the treatment delivery system used. Conventional linear medical accelerators (Elekta, Varian) are equipped with on-board imaging Cone-Beam Computed Tomography (CBCT) systems, which can operate either in 2D (kV-kV imaging) or in 3D for volumetric imaging. Peripheral imaging systems also exist, such as on the Cyberknife (Accuray) and the ExacTrac (Brainlab) delivery machines. They are based on a pair of two ceiling-mounted kV X-ray tubes at 45 degrees to the vertical and facing 2D detectors arranged in a stereoscopic geometry. The use and frequency of these imaging procedures have been growing rapidly, both to set up the patient and to track the tumor, and are fully justified by the improved target localization provided for IGRT treatments.

The downside for their increased use during IGRT protocols is the additional doses delivered to the patient. In case of intense imaging regimens (daily kV-CBCT for instance), doses to organs at risk (OAR) and normal tissues surrounding tumour site might reach 1 to 2 Gy (1) (2), with maximal doses reaching the range of 3-7 Gy (3) (4). One important feature of these additional doses is that they are delivered on a much larger volume than the therapeutic one, hence irradiating a large volume of healthy tissues. This has become a major concern for public health worldwide, called imaging dose management, which deals with several initiatives worldwide to optimize doses due to diagnostic or positioning procedures, especially for children and young adults. The case of children and young adults is of particular importance because they are much more radiosensitive than adults and that X-ray imaging-induced doses could be responsible for extra morbidity and late side effects.

Today, these additional doses delivered to the patient, as well as their potential impact on mid- and long-term increase of health risks, are poorly estimated in clinical routine. Consequently, additional imaging doses delivered are neither reported nor considered during treatment planning. This situation is worsened by the lack of a software tool for imaging dose management in radiation oncology, mainly because no legal obligation of reporting dose exists in many countries. However, scientific societies (1) (5) (2) strongly recommended to quantify and limit the patient's exposure to doses to As Low As Reasonably Achievable, following the ALARA principle. As a result, there is currently a real need of computational tools to evaluate and report imaging doses in clinical practice. This work aims to model the four previously mentioned kV imaging system using a new type of virtual source model (6) (7) (8) (9) that should enable in the future to evaluate patient specific kV-imaging dosimetry using Monte-Carlo calculations.

Material and methods

A. Description of the four kV-imaging systems

In this study, four different kV-imaging systems commonly used in IGRT protocols were modelled: the two gantry-mounted devices used for kV CBCT from Varian and Elekta linacs; and 2D kV stereoscopic orthogonal imagers on Cyberknife and ExacTrac treatment units. The major specifications of the X-ray tubes equipping each of these imaging systems are summarized in Table 1.

System	*X-ray tube*	*Anode angle*	*Inherent filtration*	*Additional filtration*	*Source to Isocenter distance*
XVI (Versa HD)		*12° (tube tilt = 3.5°)*	*3.74 mm Al + 0.1 mm Cu*	*None, Full-Fan*	*1 m*
OBI (TrueBeam)	*G-242 (Varian)*	*14°*	*5 mm Al + 0.89 mm Ti*	*None, Full-Fan, Half-Fan*	*1 m*
Cyberknife	*G-292 (Varian)*	*12°*	*3.2 mm Al*	*None*	*2.2 m*
ExacTrac	*Rad 21 (Varian)*	*12°*	*1.5 mm Al*	*None*	*2.3 m*

Table I. Systems considered in the study along with their respective specifications.

1. XVI/OBI

Two kV-CBCT systems were considered in this work, namely the On-Board Imaging (OBI) system mounted on TrueBeam linacs (Varian, Palo Alto, CA) and the X-ray Volume Imaging (XVI) system mounted on Synergy/VersaHD linacs (Elekta, Crawley, UK). Both systems are mounted orthogonally to the treatment beam axis and can operate in 2D radiography and fluoroscopy modes, and in 3D providing volumetric images of the patient. The XVI produces photon beams in the 70-120 kV range while the OBI can go up to 125 kV. Filtration and collimation are provided in two different ways on both units: latest OBI systems installed on TrueBeam linacs present bowtie filters (half-fan and full-fan) embedded directly into the X-ray irradiation unit, which is more convenient for operators, whereas for XVI systems, two removable filtration cassettes are provided, a neutral (F0) and a full-fan bowtie (F1). Collimation is also performed using removable collimation cassettes on XVI: each collimator is identified by a letter specifying the field-of-view (FOV) size (Small, Medium or Large) and a number (2, 10, 15, or 20) giving the size of the radiation field in the superior–inferior direction,

varying between 3.516 and 27.67 cm at the isocenter. The use of mobile collimators on the OBI systems allows to further adapt the FOV to the area of interest.

2. ExacTrac/Cyberknife

The Cyberknife (Accuray Inc.) (10) is an image-guided robotic system for radiosurgery and stereotactic radiotherapy, integrating a 6 MV compact linac mounted on a mobile robotic arm and a kV orthogonal imaging system that can determine in real time the target location. Treatment delivery process can be controlled using either static or fluoroscopic image acquisition, depending on the imaged anatomical site and target location. The Cyberknife system is composed of two ceiling-mounted X-ray tubes and two amorphous silicon flat-panel detectors installed on the floor, and arranged to provide orthogonal views on either side of the patient. Photon beams can be produced in the range 40-125 kV, 25-300 mA, and 1-500 ms. The collimation is fixed and set at installation.

The ExacTrac (BrainLab) is an in-room X-ray based monitoring system that detects intra-fractional tumor motion during treatment delivery, regardless of the couch angle or gantry position. Two kV X-ray units constitutes the ExacTrac system, in a similar configuration than the Cyberknife imaging system. In this case, however, the two X-ray tubes are located in the floor while the two detectors are ceiling mounted. The collimation is fixed and set at installation.

B. Monte Carlo Simulation and Phase-Space Files

The full Monte Carlo (MC) simulation of each system was carried out with the MC code PENELOPE (11) in order to calculate the photon energy fluency output distributions and store them in Phase-Space Files (PSF). Hence, a PSF was calculated for each of the different voltage and filter combinations considered in this work for each system, as summarized in Table II.

In order to generate X-ray tube output photons from primary electrons at a reasonable speed, every PSF was obtained using the forced Bremsstrahlung variance reduction technique. In practice, calculations were performed on 80 CPUs working in parallel for at least 10 hours, so that calculated PSFs contained a minimum of 10^7 photons.

System	*Filtrations and voltages*
XVI	*F0 (No filter) : 70, 80, 100 and 120 kV* *F1 (Full fan filter) : 70, 80, 100 and 120 kV*
OBI	*F0 (No filter) : 70, 75, 100, 105, 120 and 125 kV* *F1 (Full fan filter) : 100, 120 and 125 kV* *F2 (Haf fan filter) : 100, 110, 120 and 125 kV*
ExacTrac	*No filter : 80, 100, 120 and 145 kV*

Cyberknife	*No filter : 100, 110, 120 and 140 kV*

TABLE II. System configuration (filtrations and voltages) used to generate PSFs.

1. Coordinate system convention

In this study, for every X-ray tube, the coordinate system was defined so that the point of origin corresponded to the point where the primary electron beam (following the X direction) reached the anode of the X-ray tube (see Fig. 1). The resulting secondary photon beam was generated along the +Z direction. In this coordinate system, each secondary photon *i* in the beam will be defined by its position, represented by the vector **OM**, and its deviation from the Z direction was described using the angles θ and φ. Similarly, the potential deviation of the secondary photon from its initial direction was represented by the direction vector **MM'** and was expressed by the two angles θ^D and φ^D. These angles represent the amplitude and the direction of the photon deviation, respectively. The weighted distribution of θ^D values in the PSF is therefore a mean to estimate the proportion of scattered photons in the secondary photon beam.

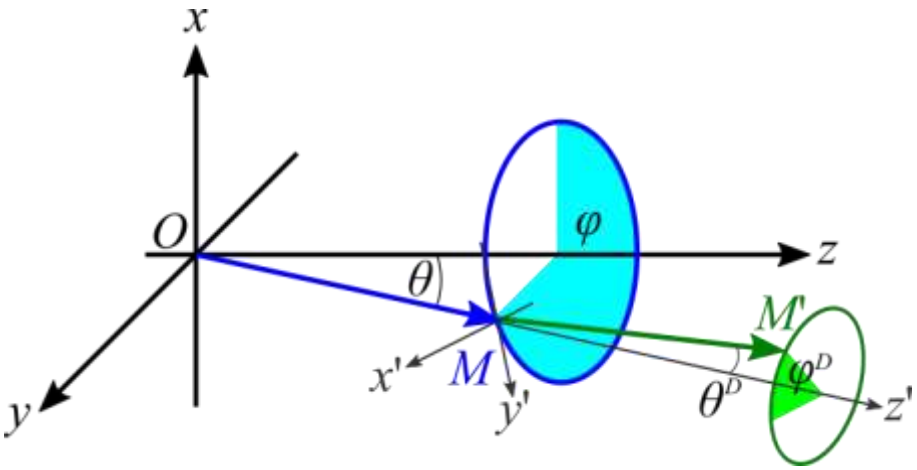

Figure 1 – Coordinate system used in the MC simulations and angle definitions for PSF analysis.

2. Photon scattering characterization

For each modelled kV beam, the angular deviation of emitted photons was analyzed from the PSF, and we observed that a very small proportion of photons were deflected following scattering. In Table III are given the highest value of the angular deviation noticed in the 9th decile distribution (first value) and in the 99th percentile distribution (values into brackets), for each imaging system and for each irradiation beam characterized by its voltage. Indeed, the highest values obtained in the 9th decile

and 99th percentile distributions of the deviation angle are equal to 0.3° and 4.8°, respectively (for the XVI system, and beam F1 : 100 kV).

	70 kV	*80 kV*	*100 kV*	*120 kV*	*125 kV*	*140 kV*
OBI-C	*No Filter : 0.1° (1.6°)*		*FF: 0.1° (2.9°) HF: 0.1° (2.2°)*	*FF: 0.1° (2.9°) HF: 0.1° (2.3°)*	*HF: 0.1° (2.5°)*	
OBI-TB	*FF: 0.1° (2.5°)*	*HF: 0.3° (3.1°)*	*FF: 0.1° (2.7°) HF: 0.1° (3.1°)*	*HF: 0.1° (2.3°)*	*HF: 0.1° (2.3°)*	
XVI	*F1 : 0.3° (4.2°) F0 : 0.3° (1.8°)*	*F0 : 0.3 (1.6°)*	*F0 : 0.1° (1.4°) F1 : 0.3° (4.8°)*	*F0 : 0.1° (1.6°) F1 : 0.3° (4.8°)*		
ExacTrac		*0.3° (3.3°)*	*0.3° (3.1°)*	*0.3° (2.9°)*		*0.3° (2.7°)*
Cyberknife			*0.1° (2.0°)*	*0.1° (0.6°)*		*0.1° (2.3°)*

Table III: Angular deviation corresponding to the 9th decile of photons (values in brackets are corresponding to the 99th percentile of photons) observed for each PSF in the study. OBI's filters are abbreviated FF (Full-Fan) and HF (Half-Fan).

C. Virtual source model

Due to the various collimation sizes and the limited number of photons in each PSF, we decided early in the study to describe the content of each PSF as a virtual source model (VSM), in which we could adapt the collimation size in a flexible and easy way. In the following, we will describe all the hypothesis and steps required to build the VSM from a pre-computed PSF.

As a starting point to build the VSM, we decided to neglect photon scattering in the different components of the X-ray tube (filter and collimator). This assumption reflects our previous observations about the very small proportion of primary photons being scattered. Consequently, the direction and position vectors **MM'** and **OM** were regarded as collinear for each photon, and θ^D and $\emptyset^D$ were considered as null. This first assumption enabled to express the planar energy fluence distribution Φ as a function of three variables, the position coordinates of the photon recorded in the PSF plane (x and y, z being identical for all photons), and its energy *E* (see equation 1)*:*

$$\Phi(x,y,E) = \Phi_0 \,.\, p_{X,Y}(x,y) \,.\, p_{E|x,y}(x,y,E) \quad \text{(Equation 1)}$$

The 2D probability function $p_{X,Y}$ and the 3D conditional probability function $p_{E|x,y}$ represent the relative intensity spatial distribution and the energy spectrum of the beam, respectively, whereas Φ_0 refers to a normalizing factor. In order to enable the expression of the planar energy fluence

distribution Φ using histogram-based functions having the smallest dimensions as possible, several assumptions were made in this work, and are now detailed.

1. Hypothesis for the energy fluence representation

First of all, the 2D spatial distribution of the photons $p_{X,Y}$ was assumed to vary independently in the X and Y directions of the beam, due to several geometrical considerations, such as the anode tilt around the Y axis (at the origin of the heel effect), the symmetry of the bowtie filters along one of the two axis, and the collimator shape and orientation. Hence, $p_{X,Y}$ can be approximated by $\tilde{p}_{X,Y}$, the product of the two 1D functions p_X and p_Y (see Equation 2).

$$p_{X,Y}(x,y) \approx \tilde{p}_{X,Y}(x,y) = p_X(x) \cdot p_Y(y) \qquad \text{Hypothesis 1} \quad \text{(Equation 2)}$$

A second hypothesis was made relative to the 3D distribution $p_{E|x,y}$ representing the energy spectrum. It was assumed that this 3D distribution could be replaced by one of the two 2D distributions $p_{E|x}$ or $p_{E|y}$ (referred in the following as $p_{E|x \text{ or } y}$), because the spectrum varies only along one of the two spatial coordinate directions of the beam, depending on the considered imaging system.

$$p_{E|x,y}(E,x,y) \approx p_{E|x \text{ or } y}(E, x \text{ or } y) = \begin{cases} p_{E|x}(E,x) \\ \text{or (depending on the system)} \\ p_{E|y}(E,y) \end{cases} \quad \text{Hypothesis 2} \quad \text{(Equation 3)}$$

Overall, these two first hypothesis enabled to simplify the expression of the planar energy fluence distribution Φ given in Eq. 1, since the initial 2D distributions $p_{X,Y}$ and 3D distributions $p_{E|x,y}$ could be expressed using two 1D spatial distributions (p_X and p_Y) and a 2D energy spectrum ($p_{E|x \text{ or } y}$), as presented in Equation 4.

$$\Phi(\mathrm{x},\mathrm{y},\mathrm{E}) \approx \widetilde{\Phi}(x,y,E) = \Phi_0 \,.\, p_X(x) \,.\, p_Y(y) \,.\, p_{E|x \text{ or } y}(x \text{ or } y, E) \text{ (Eq.4)}$$

In practice, distributions were represented as histograms containing 128 bins for p_X and p_Y , and 512 bins for $p_{E|x \text{ or } y}$.

1. VSM improvement through PSF smoothing

One major drawback linked to the use of a PSF-based simulation is that the final statistical convergence of the calculation is limited by the initial PSF size. The use of VSMs instead of PSFs for dose calculation should be helpful to limit this effect as it could be used to produce as many particles as required, without being limited in the number of created photons such as with a PSF. Nevertheless, VSMs are still limited by the noise contained in the distributions they are based on. In order to

decrease this noise, the 2D distribution $p_{E|x \text{ or } y}$ in the VSM was smoothed using a multivariate Polya Tree algorithm (12) (13) taking into account the Poisson nature of the noise affecting energy spectrum values obtained from a MC pre-calculated PSF. This algorithm also considered that there could be no abrupt discontinuities in the spectrum, except the characteristic X-rays coming from high-Z materials composing the X-ray tube anode. The smoothed version of the VSM, noted Φ^{VSM}, was therefore build from the three distributions p_X, p_Y, and $p_{E|x\ or\ y}^{smooothed}$, as given by Equation 5.

$$\Phi^{VSM}(x, y, E) = \Phi_0 \,.\, p_X(x) \,.\, p_Y(y) \,.\, p_{E|x\ or\ y}^{smooothed}(x \text{ or } y, E) \quad \text{(Eq. 5)}$$

2. VSM and virtual collimation

In this study, the collimation of each imaging system was directly modelled in the VSM, while PSFs were stored before the collimation system. In practice, photons from the PSF were sorted out depending on their geometrical location, i.e inside or outside of the FOV defined by the chosen collimation, prior building the planar energy fluence distribution Φ. This enabled to generate VSMs for multiple collimation configurations using a single PSF, which was particularly useful and convenient for the OBI system where the collimation is user-defined.

3. VSM use for dose calculation

Once the VSMs created, they can be used to generate photon beams using the following sampling procedure. The VSM is first chosen depending on the imaging system that is modelled as well as kV / filter / collimation parameters of the beam. The photon coordinates x_i and y_i are sampled from their respective integrated probability functions. Then, knowing the photon position x_i and y_i, the photon energy E_i is sampled from the smoothed 2D energy spectrum distribution using a third random number. Therefore, a photon can be generated at the position M(x_i, y_i, z_{psf}) with a direction OM(x_i, y_i, z_{psf}) and the energy E_i. If needed, it will be translated and rotated to reproduce the motions of CBCT units before being propagated within the relevant geometry (phantom or patient) with the PENELOPE MC code to compute the dose distribution.

D. Validation methodology

VSM were validated against PSF in three steps. In a first step, the validation was done directly on energy fluence distributions, as the VSM aims at representing the same data as the PSF it is based on, but in a more compact way. Second, MC dose calculations using VSMs were compared to PSF-based calculations for two study cases. Finally, VSM calculations were validated in a homogeneous phantom against measurements.

1. Verification of the VSM energy fluence distribution consistency

The energy fluence distributions described by the VSM (noted Φ^{VSM}) and by the PSF it is based on (noted Φ) were compared in order to validate the consistency of the VSM and its underlying assumptions. To this end, we chose to compare the distributions Φ^{VSM} and Φ to a reference energy fluence distribution, noted Φ_{ref}, which was obtained independently from a PSF calculated with a larger number of photons (N_{ref} equal to $3 \cdot 10^7$ photons) than the PSF from which the VSM was built (this PSF contained only N photons, with $N \leq N_{ref}$). The Hellinger distance (H_d) as defined in Equation 6 was used as the comparison metric.

$$H_d(\Phi_1, \Phi_2) = \frac{1}{2}\sum_{x,y,E}\left[\left(\Phi_1(x,y,E)\right)^{1/2} - \left(\Phi_2(x,y,E)\right)^{1/2}\right]^2 \quad \text{(Eq. 6)}$$

Additionally, the performance of the Polya smoothing process was also evaluated using the Hellinger distance to compare the two energy fluence distributions Φ^{VSM} (VSM built with the smoothed version of the energy spectrum distribution) and $\widetilde{\Phi}$ (VSM built without the Polya smoothing algorithm) with the energy fluence distribution from the reference PSF.

2. VSM-based Monte Carlo calculation consistency check

The second step of the VSM validation aimed at verifying the consistency of hypothesis done for building the VSM, by testing the capabilities of the VSM to reproduce dose calculations in water. To that end, the generic VSM established for the XVI system was tested by comparing the results of dose calculations in a water phantom based on the reference PSF and on the derived VSM. These comparisons were performed for three different beam qualities of the XVI: 120 kV F1 M20, 100 kV F0 M20, and 80 kV F0 M20.

For these tests, we considered two geometries: a mathematical anthropomorphic phantom (using the "male" geometry examples contained in the Penelope 2006 distribution) and a voxelized geometry based on the CT scan of an anthropomorphic phantom (CIRS ATOM, male). Each geometry was irradiated using each of the three XVI beams cited above (120 kV F1 M20, 100 kV F0 M20, and 80 kV F0 M20]. The number of photons stored in the PSF was equal to 10^8. The gain (G) in computation runtime provided by the use of a VSM was determined by calculating the ratio between the calculation efficiency obtained with the VSM (noted ε_{VSM}) and with the PSF (noted ε_{PSF}) (see Equation 7a). The calculation efficiency itself was defined as the inverse square of the relative uncertainty on the estimated absorbed dose (δD), divided by the total simulation time (T_{sim}, same time for both VSM and PSF based calculations) (see Equation 7b).

$$G = \frac{\varepsilon PSF}{\varepsilon VSM} \qquad \text{(Eq. 7a)}$$

$$\varepsilon_i = \frac{1}{\delta {D_i}^2 \cdot T_{sim}} \qquad \text{(Eq. 7b)}$$

3. Validation against in homogeneous phantom measurements

Dose measurements were acquired using a Farmer-type ionization chamber (PTW30013) for each of the studied X-ray imaging systems. Whenever possible, conventional dose measurements such as relative dose profiles and depth dose curves were performed in a water tank. However, these measurements needed to be adapted for the ExacTrac and Cyberknife systems because of the 45° angle of the X-ray tubes with respect to the patient couch. The different experimental conditions for each system are then described herein.

OBI, XVI. Relative dose profiles were measured in a motorized water tank (MP3 Phantom Tank, PTW). For the XVI system, three beam qualities were considered, namely, the 80 kV beam without the bowtie filter (F0), and the 120 kV beam without (F0) and with the bowtie filter (F1). Three similar beam qualities were used on the OBI system: 80 kV with the Full-Fan filter, and 120 kV with either the Full-Fan or the Half-Fan filter.

Cyberknife, ExacTrac. All measurements were performed in non-conventional phantoms mimicking in-water measurements of lateral dose profiles and depth-dose curves. Indeed, the geometrical and technical specificities of the ExacTrac and the Cyberknife imaging systems made impossible relative dose measurements following standard usual experimental setups. In practice, dose lateral profiles were measured as horizontally as possible, but with difficulties to get the exact water depth. Indeed, the use of oblique beams causes measured “depth-dose” curves to be a mixture between a standard depth-dose curve and a horizontal profile, making it difficult to draw simple conclusion from measurement. For the Cyberknife imaging system, a water tank (MP1 Phantom Tank, PTW) was used. For the ExacTrac, difficulties arise from the X-ray beam which was generated from the ground, and crossed the water tank metallic structures before reaching the dosimeter. In order to circumvent this problem, a dedicated PMMA phantom was used instead of a water tank.

For each condition of measurement, corresponding MC simulations were performed using the VSMs associated to the irradiation beam and to the imaging system, with a dose scoring volume defined with 8 mm^3 voxels. The simulated lateral dose profiles and depth dose curves were compared to experimental ones using either a global gamma-index test 3% / 3 mm (with a dose threshold set to

20% of the maximum) or a local gamma-index test 5% 5mm (without threshold) (14). Results of the test were given in terms of passing rate for both gamma-index tests.

Results

A. Validation of the description of the energy fluence distribution in the VSM

The reference PSF calculated for N_{ref} photons was used to generate two reference energy fluence distributions: Φ_{ref} was the reference raw distribution, and was stored in a PSF format, and Φ_{ref}^{VSM} was the reference VSM distribution, hence stored in the VSM format. The comparison of each test distribution with the raw reference distribution using the Hellinger distance H_d is shown in Figure 2 as a function of the PSF size.

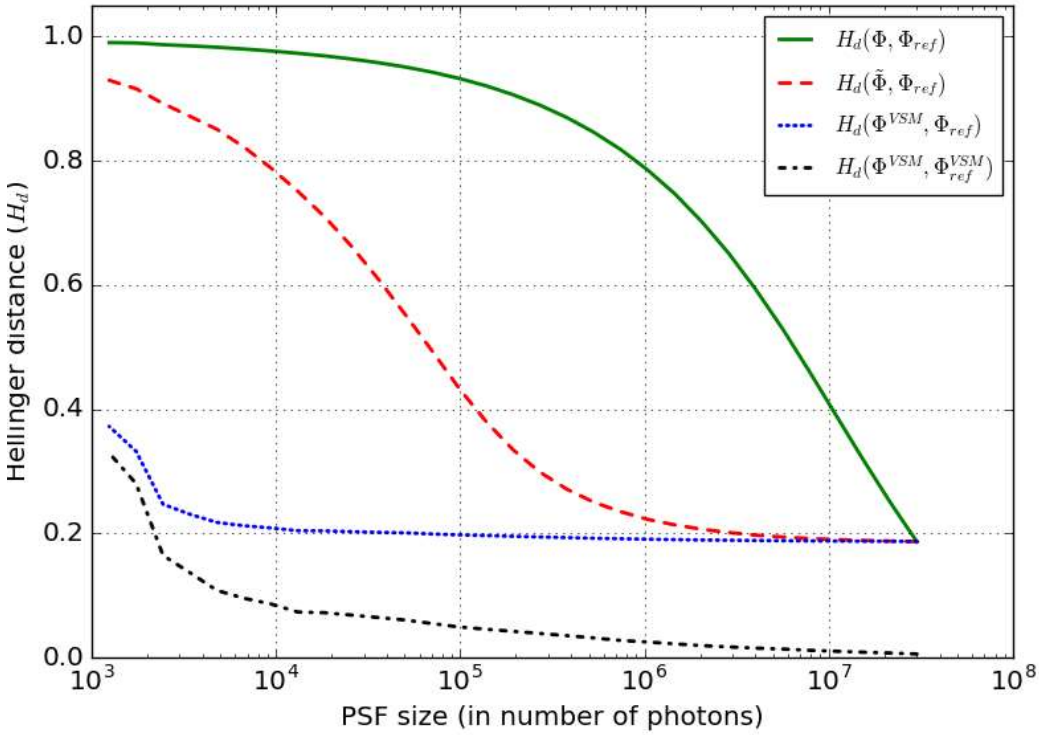

Figure 2 - Hellinger distance between the reference PSF, an independent PSF and its associated VSM (smoothed or unsmoothed) as a function of the PSF size.

The results presented in Figure 2 highlighted that the Hellinger distance between Φ and Φ_{ref} ($H_d\left(\Phi, \Phi_{ref}\right)$) was found to be very dependent on the size of the PSF from which Φ was obtained. Indeed, values calculated for the Hellinger distance reached 0.2 when N was equal to N_{ref}. In comparison, $H_d\left(\widetilde{\Phi}, \Phi_{ref}\right)$ and $H_d\left(\Phi^{VSM}, \Phi_{ref}\right)$ reached the value of 0.2 for a PSF storing 3×10^6 photons and 7×10^4 photons, respectively. This means that the distribution $\widetilde{\Phi}$ is less sensitive to the PSF size when than the PSF distribution Φ itself, and constitutes therefore a more robust estimator of the energy fluence distribution. These results also demonstrated that the Polya smoothing process applied to obtain the VSM contributed to decrease even more the dependency on the PSF size. This observation was confirmed by the fact that the Hellinger distance between Φ^{VSM} to Φ_{ref}^{VSM} went below a threshold of 0.2 with a very small number of photons (2×10^3).

Overall, we could conclude that a reliable estimation of the 3D energy fluence distribution of a VSM from a PSF required the use of a PSF storing a very large number of photons, in order to limit the statistical intrinsic noise contained in MC dose calculations. The approach proposed in this article, based on the smoothing of the energy spectrum using a Polya algorithm, allowed us to get an estimator of the energy fluence distribution in the VSM which was slightly affected by the PSF size. In other words, a pre-calculated PSF storing 2x10^3 photons was appropriate to create a robust VSM, whereas 3x10^7 are needed to obtain similar results using a PSF alone.

B. Comparison of dose calculations in water using the VSM and the PSF

Table IV summarizes the differences in dose calculations performed in the quadric and voxelized geometries. Voxels had a volume of 100 and 10 mm^3 for the quadric and the voxelized geometries, respectively. The average distances and their associated standard deviations calculated on the dose distributions simulated using a PSF and the corresponding VSM are given in two columns, one characterizing in-field doses and the other one out-of-field doses.

Geometry	Runtime (on 80 CPUs)	High Voltage (kV)	Collimation Filtration	In-field Distances (%)	Out-of-field Distances (%)	Gain	**σPSF** (%)	**σVSM** (%)
Quadric geometry		*120*	*M20 F1*	*-0.2 (σ=2.4)*	*-16.4 (σ=11.0)*	*3.4*	*1.28*	*0.73*
(v = 100 mm^3	*2h*	*100*	*M20 F0*	*0.3% (σ=2.0)*	*-4.9 (σ=4.5)*	*3.2*	*1.18*	*0.66*
5x5x4 mm^3)		*80*	*M20 F0*	*0.1% (σ=2.0)*	*-5.9 (σ=5.4)*	*2.8*	*1.12*	*0.65*
Voxelized geometry		*120*	*M20 F1*	*0.3 (σ=4.4)*	*-8.0 (σ=7.9)*	*7.8*	*2.7*	*0.98*
(v = 10 mm^3	*10h*	*100*	*M20 F0*	*0.6 (σ=4.4)*	*0.1 (σ=6.0)*	*6.7*	*2.7*	*1.0*
2.3x2.3x1.9 mm^3)		*80*	*M20 F0*	*-0.2 (σ=2.4)*	*-0.8 (σ=6.4)*	*6.0*	*2.6*	*1.1*

Table IV: Comparison of dose distributions obtained with a PSF- and a VSM-based MC calculations, in two geometries and for three beam qualities of the XVI system. Presented values of in-field and out-of-field distances correspond to the average distances and standard deviations. The simulation time gain, PSF and VSM MC uncertainties are also given for in-field values.

The presented in-field dose standard deviation (doses higher than 20% of the maximum dose) between PSF and VSM based MC calculations are below 2.4% and 4.4% respectively for the 100 mm^3 and 10 mm^3 geometries, while the mean dose distance is below 0.6%. Such values are compatible with the MC calculation uncertainty.

By contrast, dose distance values reported out-of-field stressed out that the dose distribution was underestimated by 5 to 17% in the 100 mm^3 voxel geometry when calculated by the VSM, with the largest underestimation observed for the 120 kV beam (cf Figure 3). This could be explain by the fact the diffusion was neglected and that virtual collimation was used when constructing the VSM. Indeed, they both stated that there was no out-of-field photon emitted from the X-ray tube and therefore that only in-body diffusion contributed to out-of-field dose.

Due to higher noise in the 10 mm^3 geometry (linked to the smaller size of the voxels), the out-of-field dose comparison are less conclusive especially at 100 and 80 kV.

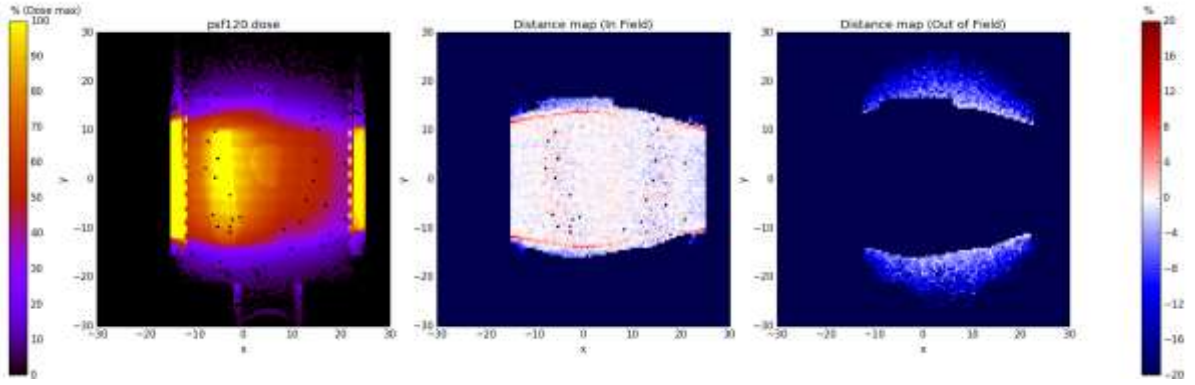

Figure 3 – Comparison of dose maps obtained with the PSF and the VSM, in and out-of-field for the 120 kV beam irradiating the quadric geometry.

E. Experimental validation in a water phantom

Table V shows a summary of the global and local gamma-index passing rates obtained from the comparison between VSM-based dose calculations (smoothed version) and measurements, for all

tested irradiation beams of the four imaging systems. Overall most of the data displayed agreement above the 90% threshold, with the lowest passing rate obtained at 84.1%. Such passing rate values might be seen as low in radiotherapy assurance quality, but here, they rather put into the light the difficulties met to measure low dose areas located out of the imaging FOV. Considering the level of dose accuracy that is required in this application, obtained results could be acceptable. All corresponding profiles and depth-dose curves are presented in Appendix 1.

Imaging system	Irradiation beam setup	$\Gamma_L 5\%\ 5\ \mathrm{mm}$ *(%)*	$\Gamma_G 3\%\ 3\ \mathrm{mm}\ (T = 20\%)$ *(%)*
XVI	*120kV Full Fan S20*	*93.3*	*94.0*
	120 kV S20	*94.0*	*90.1*
	80 kV M20	*88.9*	*90.3*
OBI	*125kV Half-Fan*	*87.2*	*91.8*
	125kV Full-Fan	*89.7*	*96.9*
	80kV Full-Fan	*89.2*	*90.9*
Cyberknife	*140 kV*	*94.0*	*87.5*
	100 kV	*92.5*	*84.9*
ExacTrac	*145 kV*	*88.2*	*91.3*
	80 kV	*96.1*	*84.1*

Table V: Passing rates for each configuration tested on the four imaging systems, using either local gamma index (5% / 5mm) or global gamma-index (3% / 3mm, with a 20% dose threshold).

Conclusion

To conclude, this study highlighted the possibility to use VSM in order to fasten and simplify MC-based dose calculation in kV-imaging. Indeed, compared to standard PSF based calculations, the use of VSM enabled to decrease the computation time by at least 2.8 for the same statistical uncertainty. The presented method also enabled to take in account the actual collimation size used during the kV-imaging procedure without a remodeling of the physical collimation. Nevertheless, this flexibility as a cost when looking at out-of-imaging-field doses, and such doses tended to be underestimated by up to 20%. This might not be an issue, as out-of-imaging-field doses are by definition negligible, but it should be kept in mind when using such technique.

This methodology was applied on four of the main clinically available IGRT tools (two kV-CBCT: OBI and XVI; two 2D-kV imaging systems: CyberKnife and ExacTrac). Simulated profiles and depth dose curves were compared to in homogeneous phantom measurements and showed a good agreement (above 90% at the global 3% 3 mm gamma-index test).

To validate fully the use of VSM for kV-imaging dosimetry, we will in the future conduct new sets of measurements using anthropomorphic phantoms and standard kV-imaging procedures.

Acknowledgments

This work was financially supported by the French National Research Agency (ANR) project Additional Imaging Doses and associated risks in Image-Guided Radiotherapy (AID-IGRT) (ANR-15-CE19-009).

Bibliography

1. *The management of imaging dose during image-guided radiotherapy: Report of the AAPM Task Group 75.* **Murphy, M. J., Balter, J. , Balter, S. , BenComo, J. A., Das, I. J., Jiang, S. B., Ma, C. , Olivera, G. H., Rodebaugh, R. F., Ruchala, K. J., Shirato, H. and Yin, F.** 2007, Medical Physics , Vol. 34, pp. 4041-4063.

2. *Image guidance doses delivered during radiotherapy: Quantification, management, and reduction: Report of the AAPM Therapy Physics Committee Task Group 180.* **Ding, George X., et al.** 5, 2018, Medical Physics, Vol. 45.

3. *Radiation Dose From Kilovoltage Cone Beam Computed Tomography in an Image-Guided Radiotherapy Procedure.* **Ding, George X. and Coffey, Charles W.** 2, International Journal of Radiation Oncology Biology Physics : s.n., 2009, Vol. 73, pp. 610-617.

4. *Patient-Specific Three-Dimensional Concomitant Dose From Cone Beam Computed Tomography Exposure in Image-Guided Radiotherapy.* **Spezi, Emiliano, et al.** 1, 2012, International Journal of Radiation Oncology Biology Physics, Vol. 83.

5. *American Society for Therapeutic Radiology and Oncology (ASTRO) and American College of Radiology (ACR) Practice Guidelines for Image-Guided Radiation Therapy (IGRT).* **Potters, Louis, et al.** 2, 2010, International Journal of Radiation Oncology Biology Physics, Vol. 76, pp. 309-325.

6. *A virtual source model for Kilo-voltage cone beam CT: Source characteristics and model validation.* **Spezi, E. and Volken, W. and Frei, D. and Fix, M. K.** 9, 2011, Medical Physics, Vol. 38, pp. 5254-5263.

7. *Development and implementation in the Monte Carlo code PENELOPE of a new virtual source model for radiotherapy photon beams and portal image calculation.* **Chabert, I., et al.** 14, 2016, Physics in Medicine & Biology, Vol. 61.

8. *Experimental validation of a kV source model and dose computation method for CBCT imaging in an anthropomorphic phantom.* **Poirier, Yannick and Tambasco, Mauro.** 2016, Journal of Applied Clinical Medical Physics, Vol. 17, pp. 155-171.

9. *A measurement-based generalized source model for Monte Carlo dose simulations of CT scans.* **Ming, Xin, et al.** 5, 2017, Physics in Medicine & Biology, Vol. 62.

10. *The CyberKnife® Robotic Radiosurgery System in 2010.* **Kilby, W., Dooley, J. R., Kuduvalli, G., Sayeh, S., & Maurer, C. R.** 2010, Technology in Cancer Research & Treatment, pp. 433–452.

11. **Francesc Salvat, José M. Fernández-Varea, Josep Sempau.** *PENELOPE-2006: A Code System for Monte Carlo Simulation of Electron and Photon Transport ISBN: 92-64-02301-1 Francesc Salvat, José M. Fernández-Varea, Josep Sempau Facultat de Física (ECM) Universitat de Barcelona Spain.* 2006. ISBN 92-64-02301-1.

12. *The Polya Tree Sampler: Towards Efficient and Automatic Independent Metropolis-Hastings Proposals.* **TE, Hanson, JV, Monteiro and A, Jara.** 1, 2011, Hanson, Timothy E et al. “The Polya Tree Sampler: Towards Efficient and Automatic Independent Metropolis-Hastings Proposals.” Journal of computational and graphical statistics : a joint publication of American Statistical Association, Institute of Mathema, Vol. 20, pp. 41-62.

13. *Robustifying Generalized Linear Mixed Models Using a New Class of Mixtures of Multivariate Polya Trees.* **Jara, Alejandro, Hanson, Timothy E. and Lesaffre, Emmanuel.** 2009, Journal of Computational and Graphical Statistics, Vol. 18, pp. 838-860 .

14. *A technique for the quantitative evaluation of dose distributions.* **Low, Daniel A., et al.** 5, Medical Physics, Vol. 25, pp. 656 - 661.

Appendix 1

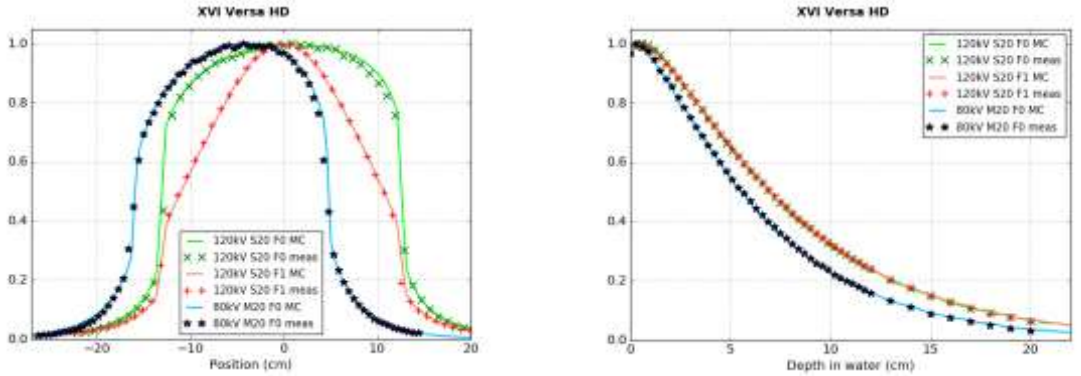

Figure 3: XVI Versa

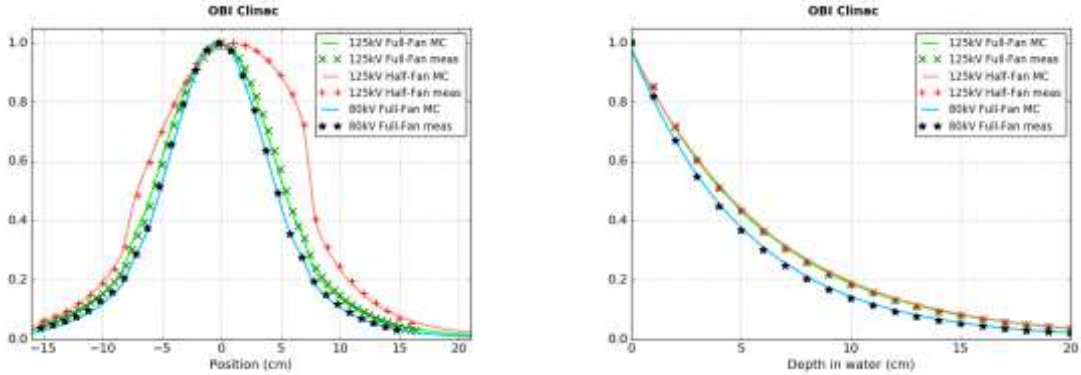

Figure 4: OBI Clinac

Figure 5: Cyberknife

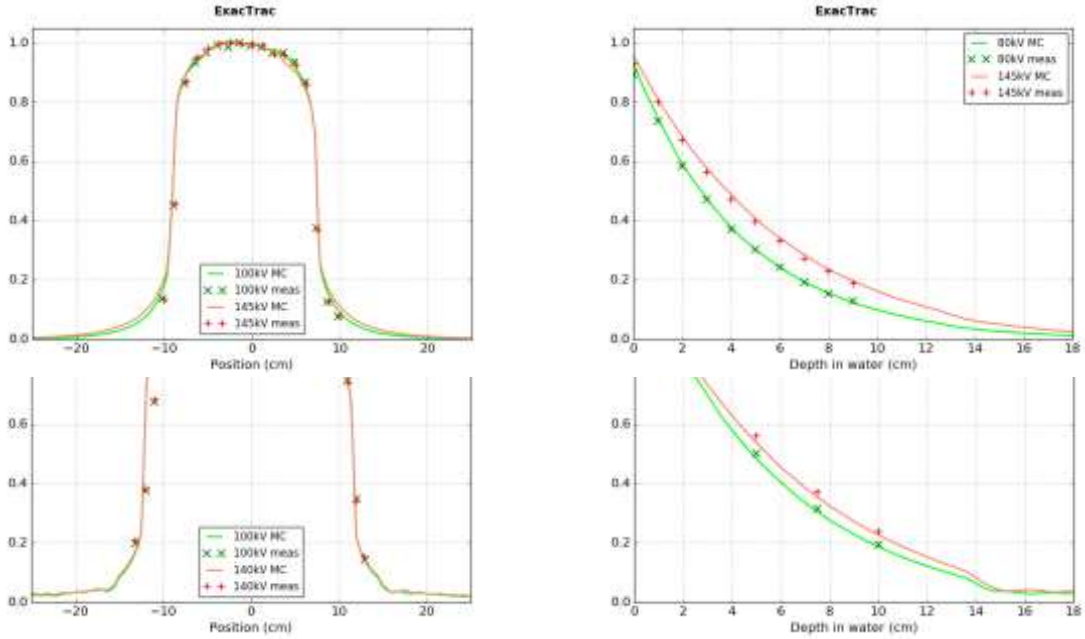

Figure 6: ExacTrac